# Correction of Interferometric High-Order Nonlinearity Error in Metrological Atomic Force Microscopy

Gaoliang Dai[1] · Xiukun Hu[2]

## Abstract

Metrological atomic force microscopes (Met. AFMs) with built-in interferometers are one of the main workhorses for versatile dimensional nanometrology. The interferometric nonlinearity error, particularly the high-order (i.e., 3rd- and 4th-order) nonlinearity errors, is a dominant error source for further improving their metrology performance, which cannot be corrected using the conventional Heydemann correction method. To solve this problem, two new methods were developed. One uses a capacitive sensor embedded in the Met. AFM, and the other applies an external physical artifact with a flat surface. Both methods can be applied very conveniently and can effectively reduce the nonlinearity error. In this paper, the propagation of the (residual) nonlinearity error in step height calibrations is examined. Finally, the performance of the improved tool is verified in the calibration of a highly demanding industrial sample. For the measurements performed at 25 different positions and repeated six times, the standard deviation of the total 150 measured values is 0.08 nm, which includes the contributions from the reproducibility of the metrology tool and sample inhomogeneity. This research has significantly improved our dimensional nanometrology service. For instance, the extended measurement uncertainty ($k = 2$) is reduced from 1.0 to 0.3 nm for the step height or etching depth calibrations.

## 1 Introduction

Nanometrology is key to innovations in nanotechnology and nanoscience, such as understanding the interaction mechanism between atoms, controlling nanomanufacturing processes, optimizing nanoscale products, and preventing nanotoxicity. To satisfy various nanometrology demands, a wide range of nanometrology techniques with different underlying physics, including optical, ion, electron, X-ray, and surface forces, have been developed. For instruments based on any of these underlying techniques, traceable nanometrology plays an essential role in producing accurate results, ensuring the quality of measurements, and enhancing tool-to-tool

matching. As such, traceability is a fundamental issue for nano-dimensional metrology, and its absence inhibits the comparison of tools from different manufacturers and limits knowledge about the real size of fabricated features [1].

The calibration of nanometrology tools using proper physical standards is a typical approach for ensuring their measurement traceability [2]. Such physical standards include the step height, one-dimensional/two-dimensional (1D/2D) gratings, or three-dimensional (3D) pyramid standards, which are available for calibrating the scaling factors of the vertical and lateral axes of nanometrology tools [3]. Prior to their usage, these physical standards are usually calibrated using metrology tools, such as diffractometer [4] (for lateral standards), interference microscopy [5] (for height standards), or metrological atomic force microscopes (Met. AFMs) [6–9] with built-in interferometers (for lateral, height, and 3D standards). According to the wave optic theory, the measurement results of these metrology tools can be directly related to the wavelength ($\lambda$) of the applied optical source, which can in turn be linked to the SI unit meter, as the optical frequency is calibrated either to an iodine frequency stabilized laser or an optical frequency comb

✉ Gaoliang Dai
gaoliang.dai@ptb.de

1 Physikalisch-Technische Bundesanstalt, Bundesallee 100, 38116 Braunschweig, Germany

2 Key Laboratory for Magnetism of Zhejiang Province, College of Materials and Chemistry, China Jiliang University, Hangzhou 310018, People's Republic of China

[10]. Through such an unbroken calibration chain described above, the traceability of the dimensional properties of nanostructures can be ensured.

The accurate and traceable calibration of the step height and/or etching depth of micro- and nanostructures is one of the most fundamental and industrially demanded calibration tasks in nanometrology. Today, Met. AFM is one of the most accurate methods for step height calibrations, which offers a typical expanded measurement uncertainty $U$ of 1.0–2.0 nm ($k = 2$), as confirmed by the international comparison NANO2 [11]. However, there are increasing requirements on the reduction of $U$ to below 0.5 nm (0.3 nm desired) by some industrial sectors, such as the metrology of the absolute feature heights of photomask structures and diffractive optical elements for the simulation and thus control of their (optical) functions. Accordingly, reducing the measurement uncertainty of the state-of-the-art Met. AFMs demands challenging research.

To further improve the measurement accuracy of Met. AFM, a thorough study has recently been performed at the Physikalisch-Technische Bundesanstalt (PTB), the national metrology institute of Germany. Three aspects were reviewed with great care as they are the most susceptible factors of measurements: (1) nonlinearity errors of interferometers, (2) ghost interference fringe present in the AFM optical detection system, and (3) form deviation of the measurement mirrors of optical interferometers. The results of our study indicate that the nonlinearity errors of interferometers are still the most dominant error source, particularly due to the presence of higher-order (i.e., 3rd- and 4th-order) components in the nonlinearity errors of interferometers. Finally, this study leads to significant progress in our nanometrology calibration capability: a reduction of measurement uncertainty for the step height and etching depth calibrations from $U > 1.0$ nm to 0.3 nm.

This paper aims to introduce the progress made as mentioned above. It consists of six sections. Section 2 shortly introduces the principle of our Met. AFM and the presence of high-order interferometric nonlinearity error. Section 3 details two methods developed for the characterization and correction of the high-order nonlinearity error. Section 4 examines the error propagation of the (residual) nonlinearity error in the step height and etching depth calibrations. Section 5 demonstrates the performance of the step height and etching depth calibration after improvements. This paper is an extended version of our previously published extended abstract in the proceeding of the EUSPEN conference [12].

## 2 Principle of the Met. LR-AFM and Its High-Order Interferometric Nonlinearity Error

A metrological large-range AFM (Met. LR-AFM) has been successfully set up at the PTB since 2004 [13] based on a high-precision stage referred to as a nanomeasuring machine (NMM) [14]. The setup of the Met. LR-AFM is illustrated in Fig. 1a. The sample (S) to be measured was fixed to the motion platform of a piezo stage (PZT-stage). The PZT stage was in turn mounted on the motion platform of the NMM, which is the mirror corner, as shown in the figure. Three stacked mechanical stages ($x$-, $y$-, and $z$-stages) driven by voice coil actuators were applied to move the mirror corner. The six-degrees-of-freedom position of the mirror corner was measured by three interferometers and two autocollimators embedded in the NMM. Only the interferometers for the measurements of displacements along the $x$- and $z$-axes ($x$-Interf and $z$-Interf) are depicted in Fig. 1a, but the $y$-Interf and two laser autocollimators are not shown for clarity. To reduce Abbe error, the AFM tip was positioned at the intersection point of three measurement beams of interferometers. One frequency stabilized He–Ne laser was used as the light source for all interferometers. Its optical frequency was calibrated at $632\ 991\ 234 \pm 5$ fm by the optical frequency standard available at the PTB, ensuring direct traceability for the measurements.

The Met. LR-AFM operates in the so-called scanning sample principle. The sample was moved in the $xy$-plane at the given scan speed solely by the NMM, whereas along the $z$-axis, it was moved by two stages (i.e., the PZT-stage and NMM) using a cascade servo controller during the measurements. This cascade servo controller simultaneously runs a fast servo loop and a slow servo loop. The fast servo loop quickly moves the sample up- or downward by the PZT-stage to keep the AFM tip–sample interaction constant, whereas the slow servo loop moves the PZT-stage (together with the sample) up- or downward by the $z$-motion of the NMM so that the motion of the PZT-stage is controlled toward its predefined home position. With this novel design concept of the dual-stage and cascade servo controller, the Met. LR-AFM has the advantages of a large measurement range and high measurement speed (please refer to [13] for more details). The nanostructure geometry can be derived from the $x$-, $y$-, and $z$-motions of the two stages. For instance, the $z$-coordinate of the AFM pixels was calculated from the outputs of the AFM signal, the output of the capacitive sensor embedded in the piezo stage for measuring its $z$-motion, and the value of the $z$-Interf of the NMM, which were simultaneously acquired [15]. Before the measurements, the capacitive sensor and AFM signal were traceably calibrated to the interferometers of the NMM [13]. The Met. LR-AFM, with
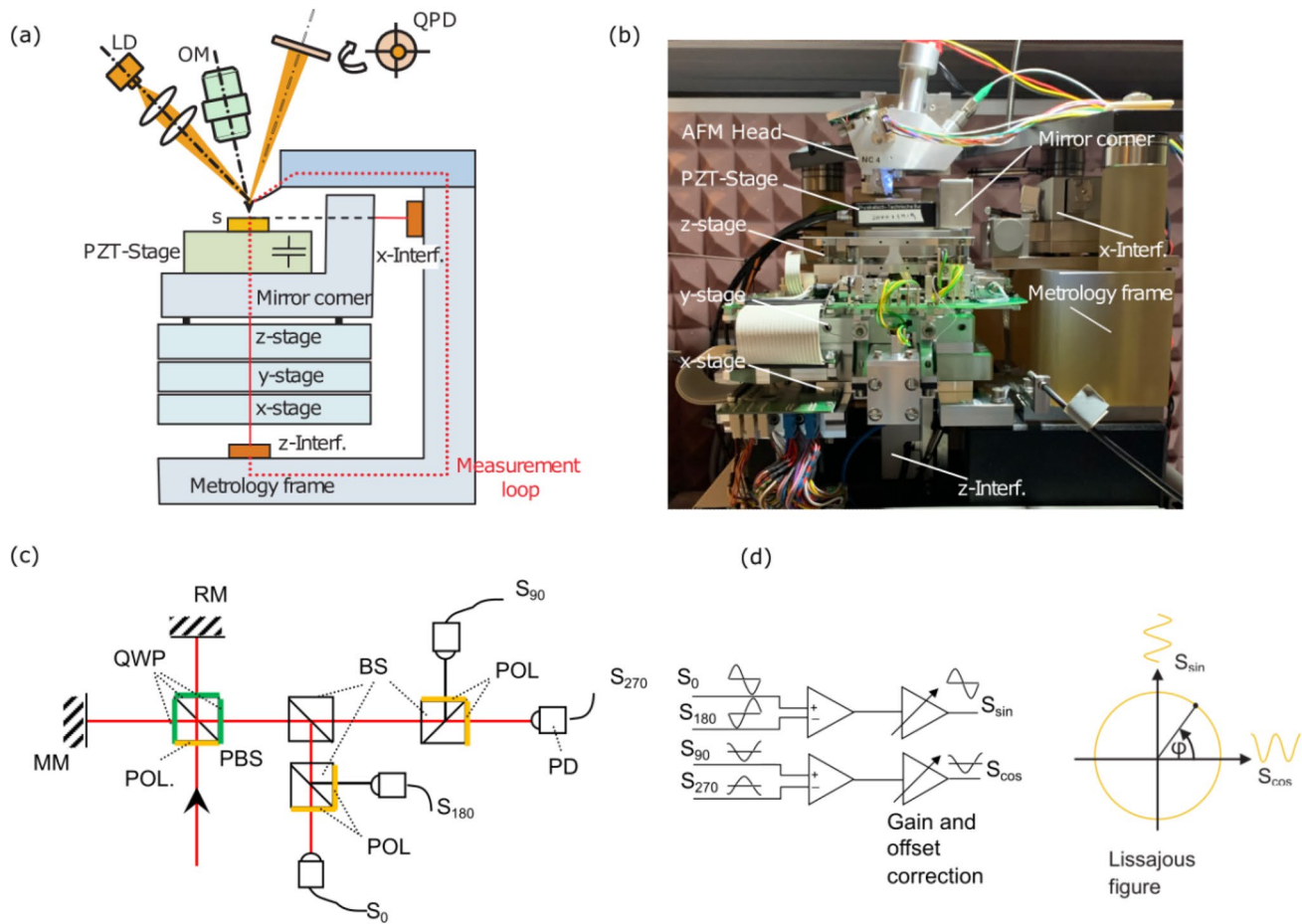
**Fig. 1** **a** Schematic diagram of the metrological large-range atomic force microscope (Met. LR-AFM) at the PTB; **b** photo of the device; **c** measurement principle of the interferometer; **d** principle of the demodulation of interferometer signals

a capable measurement volume of 25, 25, and 5 mm along the *x*-, *y*-, and *z*-axes, respectively, is now a multifunctional and unique workhorse for versatile dimensional nanometrology tasks at the PTB. A photo of the measurement setup is shown in Fig. 1b.

To understand the phenomenon of the cyclic nonlinearity error, the measurement principle of the interferometers is shown in Fig. 1c. It is a kind of homodyne planar-mirror Michelson-type interferometer. After the incident laser source was polarized by a polarizer (POL), it was split by a polarizing beam splitter (PBS) into a reference beam and measurement beam with linear *s*- and *p*-polarizations, respectively. The polarization state of the reference beam changed to a circular polarization after the beam passed through a quarter-wave plate (QWP), whose fast axis was oriented at 45°. The beam was returned after being reflected by a reference mirror (RM). After passing the QWP for the second time, it changed into a linear *p*-polarization beam and thus was reflected at the PBS. Similarly, the measurement beam passed through a QWP was reflected by the

measurement mirror (MM) and passed the QWP for the second time. It changed into a linear *s*-polarization beam and passed through the PBS. Thus, the returned measurement and reference beams recombined after the PBS. The recombined beam was split using normal beam splitters into four detection beams. After passing POL, they were detected by four photodetectors (PD). By adjusting the orientation of the polarization axis of the POL, four detection signals, i.e., $S_0$, $S_{90}$, $S_{180}$, and $S_{270}$, with phase shifts of 0°, 90°, 180°, and 270°, respectively, can be obtained. Their demodulation is shown in Fig. 1d. The differential signals of $S_0$–$S_{180}$ and $S_{90}$–$S_{270}$ were first obtained to reduce the DC offsets of the detection signals. They were then amplified with an adjustable gain and offset to obtain a pair of quadric interferometer signals $S_{cos}$ and $S_{sin}$. Ideally, the Lissajous figure of this signal pair is circular, as shown in Fig. 1d, from which the phase ($\varphi$) can be determined. The displacement can then be calculated as

$$L = \frac{\lambda_{\text{Laser}}}{2n}\left(m + \frac{\varphi}{2\pi}\right), \tag{1}$$

where $\lambda_{\text{Laser}}$ is the vacuum wavelength of the laser source, $n$ is the refractive index of air, $m$ is the integer part of the counted interference fringes, and $\varphi$ is the fractional part of the interference fringe.

To have an ideal circular Lissajous trajectory, as mentioned above, the quadratic interferometer signals $S_{\text{cos}}$ and $S_{\text{sin}}$ should have zero offsets, identical amplitudes, and an exact 90° phase difference. However, in practice, many factors, such as polarization mixing (e.g., due to the imperfect components QWP, PBS, and POL), unwanted light reflection (e.g., at the surface of QWPs), laser beam misalignment, imperfection of electronic processing, and error motion of stage, may inevitably distort the interference signal from the ideal case. Consequently, it results in a well-known issue of interferometric nonlinearity errors. Such nonlinearity errors are cyclic at the frequency of $(2n/\lambda_{\text{Laser}})$ and/or its harmonic frequencies.

In our previous study [16], we applied the Heydemann correction method [17] to correct such a nonlinearity error. The relationship between the distorted and ideal interferometer signals is modeled as follows [16]:

$$\begin{aligned} u_1^d &= u_1 + p \\ u_2^d &= \frac{1}{r}\left(u_2 \cos\alpha - u_1 \sin\alpha\right) + q, \end{aligned} \tag{2}$$

where $(u_1^d, u_2^d)$ indicates a vector of the distorted quadratic interferometer signal, and $(u_1, u_2)$ indicates a vector of the ideal quadratic interferometer signal.

In applying the Heydemann correction method, the MM was slightly moved, and a Lissajous trajectory of $(u_1^d, u_2^d)$ was recorded. It was then least-square-fit to an ellipse so that the model parameters of $p, q, r$, and $\alpha$ in Eq. (2) can be calculated. With these model parameters, the ideal vector $(u_1, u_2)$ can be calculated using Eq. (2) from the measured vector $(u_1^d, u_2^d)$. Using this method, we effectively reduced the nonlinearity error to less than 0.3 nm for the metrological AFM type "Veritekt C" in our previous study [16].

However, the Heydemann correction method mentioned above is insufficient to correct the nonlinearity errors of the Met. LR-AFM. To illustrate this problem, the Lissajous trajectory of the measured raw signals of the $z$-interferometer of the Met. LR-AFM is plotted in Fig. 2a. After performing the Heydemann correction, the Lissajous trajectory of the corrected interferometer signals is shown in red in Fig. 2b, where it is zoomed in the radial axis for clarity. Clearly, it significantly deviates from an ideal circular shape (shown in blue). The deviation is also depicted in Fig. 2c, where the phase angle is plotted as the positive $x$-axis. Four periods are visible in the phase range
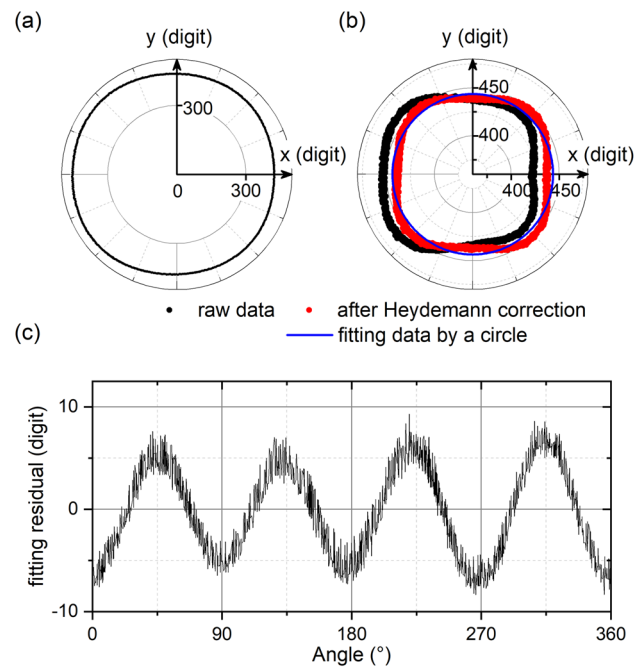


**Fig. 2** High-order nonlinearity error appears in the $z$-interferometer of the Met. LR-AFM, which cannot be corrected using the Heydemann correction method, shown as **a** raw data; **b** Heydemann corrected data (*red*) and its fitted ideal circle (*blue*); and **c** deviation of the Heydemann corrected data from its fitted circle, which indicates the presence of the 4th-order nonlinearity error

of 360°, indicating the presence of the 4th-order nonlinearity error. The deviation has a peak–peak amplitude of about 12 digits, which corresponds to approximately 2.6% of the intensity of the interferometer signal (~450 digits), resulting in nonlinearity errors of > 1 nm and thus significantly impacting the measurement uncertainty of the Met. LR-AFM.

## 3 Characterization and Correction of High-Order Nonlinearity Errors

The characterization and correction methods of the interferometric nonlinearity error can be generally divided into two categories. The first category is the fitting and correction of the Lissajous trajectory of interferometer signals based on a theoretical model that describes the relationship between ideal and distorted interferometer signals. The Heydemann correction mentioned above is a method of this category that is based on the model described by Eq. (2). This method needs no external sensors or standards and is therefore convenient to be applied. However, using this method, the theoretical model must correctly describe the real system. If it is not the case, an ideal quadratic interferometer signal cannot be recovered from the measured signal, and consequently

a significant correction error will happen, as illustrated in Fig. 2. The second category is the characterization of interferometers using an additional sensor. Such a sensor could be, for instance, a constant motion velocity, a kind of displacement sensor, or a geometric standard. In addition, such a sensor could be either an internal sensor available in the measurement system or an external sensor that needs to be applied whenever a characterization is needed. The advantage of this category lies in the fact that no theoretical model is needed. Thus, it is particularly feasible for correcting nonlinearity errors with complicated phenomena where the physical reasons underpinning a nonlinearity error are unclear. As a drawback, it needs an additional sensor whose performance will impact the accuracy. As a good example of the second category, Bridges et al. recently reported interferometry operated with laser sources with two wavelengths (632.8 and 785 nm), where the interferometer values operated at different wavelengths are compared with one another for separating their nonlinearity errors with a Fourier approach [18].

Despite the considerable efforts spent in analyzing the origin of the higher-order nonlinearity error in the interferometers of the Met. LR-AFM, we failed to set up a satisfying theoretical model needed for correcting the nonlinearity errors. Therefore, we developed new methods of the second category for the correction of nonlinearity errors. In this study, two kinds of sensors/standards were applied. One is a kind of physical artifact with a flat surface, e.g., a glass or silicon flat. The other is an embedded capacitive sensor in the PZT stage of the Met. LR-AFM.

### 3.1 Characterization of the High-Order Nonlinearity Error Using a Flat Surface

Figure 3 illustrates the characterization of the nonlinearity error of the $z$-axis interferometer using a glass flat. The $z$-interferometer is focused here as it is usually the most important axis for AFM measurements. The sample was mounted in the Met. LR-AFM with a slight tilting angle (approximately 0.6°) in the $xz$ plane. This tilting angle was introduced intentionally, so that the titled flat surface can act as a linear "sensor" along the $z$-axis. The AFM measurements were performed with the $x$-axis as the fast scan axis. A typical AFM topography image as the raw measurement data is shown in Fig. 3a. It was least-square-fitted to an ideal plane, and the fitting residual is plotted in Fig. 3b. Cyclic artifacts can be observed. Such artifacts may be attributed to several contributions, such as (1) the nonlinearity error of the $z$-interferometer, (2) the form error of the sample surface, (3) ghost artifacts that might be introduced by the AFM measurements, and (4) measurement noise. Although the outputs of the AFM signal and capacitive sensor are also applied in calculating the height values of the measured

surface topography, they are almost constant in the measurement of flat surfaces and thus have little contribution to the observed artifacts.

Owning to the cyclic nature of the interferometric nonlinearity error, the interferometric nonlinearity error can be separated from other contributions. The AFM image was processed line-wisely. After linearly fitting the measured profile, its deviation curve is plotted as the black curve in Fig. 3c. The curve was trimmed so that the height span of the curve is an integer time of $\lambda_{\text{Laser}}/2n$, as indicated on the top axis of Fig. 3c, to reduce the so-called window effect of the Fourier transformation (FT). It can then be processed using the FT to determine the nonlinearity error. The calculated FT result is shown in Fig. 3d. It contains frequency components with frequencies $f = 2nk/\lambda_{\text{Laser}}$ (where $k = 1, 2, 3, 4, \ldots$), as marked in red, which can be regarded as the nonlinearity error of the $z$-interferometer. The remaining frequency components are shown in black, which can be attributed to the other contributions. The red-marked frequency components can be inverse-Fourier-transformed to calculate the nonlinearity error curve, as illustrated in the red curve in Fig. 3c. This curve can then be applied as a look-up table for the correction of the nonlinearity error, as will be introduced later. Furthermore, Fig. 3c and d show that the interferometer has a dominant 4th-order nonlinearity error, agreeing well with our observation shown in Fig. 2c.

Nonetheless, there is a fundamental issue left after applying the method introduced above: "what is the influence of the surface quality on the nonlinearity characterization?" The reason is that the sample surface may also contain frequency components that overlap with those of nonlinearity errors. To investigate this issue, we characterized the $z$-interferometer using five different silicon and glass samples with a surface roughness value $R$a of approximately 2 nm. Such samples are easily obtainable, e.g., from a glass substrate or blank silicon wafer. The characterized nonlinearity error curves are compared in Fig. 4a. They agree well with one another. The standard deviation is approximately 0.1 nm and reaches 0.22 nm at its maximum. It is (much) smaller than the roughness value of the applied surface. The reason lies in the fact that only the spatial frequency components of the surfaces, which exactly overlap with the cyclic frequency components of nonlinearity errors, will contribute to the deviation.

To further study the impact of the sample's surface quality on the characterization performance of the nonlinearity error, we applied a super flat surface made of a single crystal plane of silicon. Its surface roughness $R$a is (much) less than 0.3 nm. Six measurements were performed at different locations on the same surface and with different measurement parameters and AFM probes. The obtained six nonlinearity error curves are plotted in Fig. 4b. The standard

**Fig. 3** Characterization of the high-order nonlinearity error of the *z*-interferometer using a flat surface. **a** Measured raw data of the flat surface. **b** Residual topography after applying a planar fitting. **c** Measured (*black*) and calculated (*red*) nonlinearity errors. **d** FT results, where the harmonic nonlinearity error components are shown in *red*
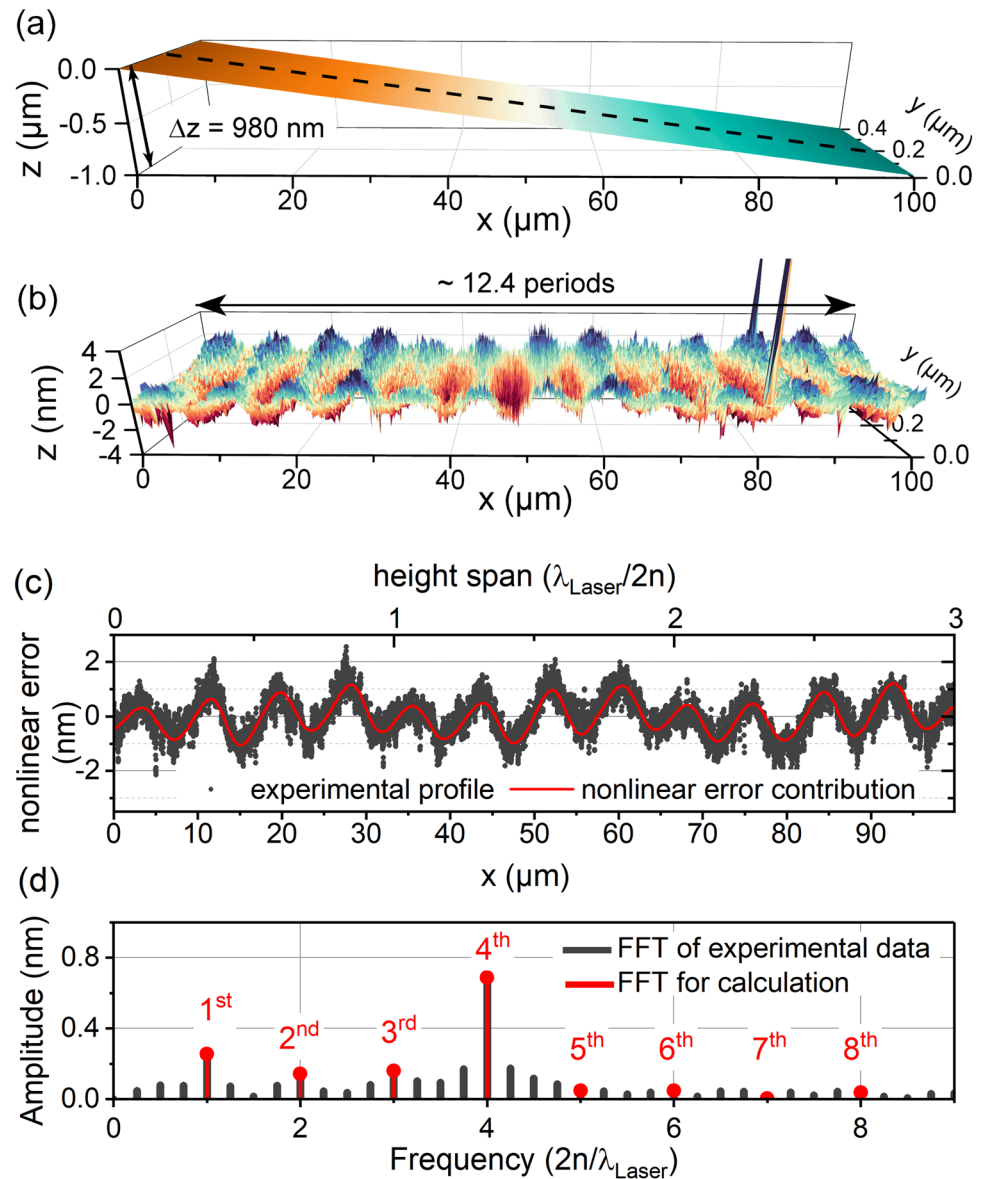


deviation of the determined nonlinearity error curves is below 0.03 nm, indicating the excellent performance of the proposed method.

The averaged nonlinearity curves from Fig. 4a and b are compared in Fig. 4c, showing an excellent agreement. This result confirms not only the feasibility of our proposed method but also the high stability of the nonlinearity behavior of the interferometer. Such behavior is expected in our Met. LR-AFM owing to its stable mechanical and optical constructions.

## 3.2 Characterization of the High-Order Nonlinearity Error Using the Embedded Capacitive Sensor in the PZT-Stage

The characterization of the high-order nonlinearity error using the embedded capacitive sensor (refer to Sect. 2) can be carried out in situ. After landing an AFM tip onto a sample surface, the AFM servo control was activated so that the tip–sample interaction (distance) is kept constant. The sample was then moved in the *z*-direction by the NMM for a given distance (e.g., $2n\lambda_{Laser}$) while keeping its *x* and *y* positions unchanged. At the same time, the PZT stage was commanded by the AFM servo controller to track the motion of the NMM and keep the tip–sample distance constant. As a fixed point on the sample was measured by the AFM tip, according to the measurement loop shown in
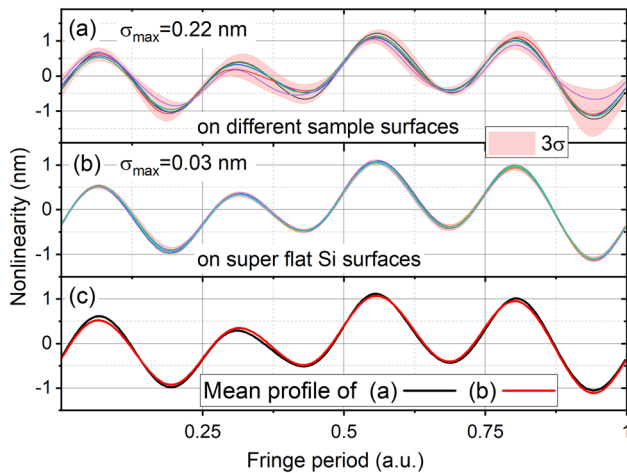
**Fig. 4** Nonlinearity error curves of the $z$-interferometer characterized using different flat surfaces: **a** Five curves characterized by five different glass and silicon flats with $R$a of approximately 2 nm. **b** Six curves characterized by an ultra-fine crystal silicon surface with $R$a < 0.3 nm. **c** Comparison of the averaged nonlinearity error curves obtained in **a** and **b**
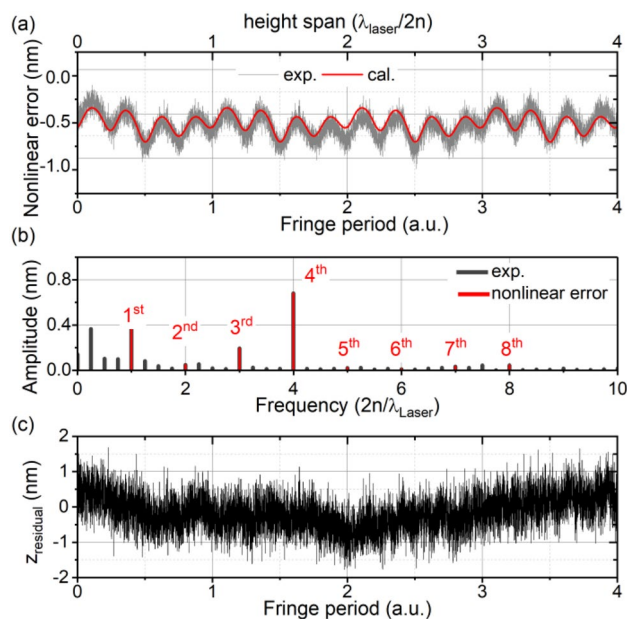


**Fig. 5** Characterization of the high-order nonlinearity error of the $z$-interferometer using the embedded capacitive sensor, shown as **a** the nonlinear deviation curve between the readout of the capacitive sensor and the value of the $z$-interferometer; **b** FT results, where the harmonic nonlinearity components of the $z$-interferometer are shown in red; and **c** residual curve after removing the nonlinearity error of the $z$-interferometer, which includes the contribution of the nonlinearity of the capacitive sensor and tracking error

the characterization process, the $z$-interferometer and capacitive sensor could be characterized.

As an example, after a measured curve using the method mentioned was taken, its nonlinear deviation curve was calculated and shown in Fig. 5a. This nonlinear curve mainly includes two contributions: nonlinearities of the $z$-interferometer and the capacitive sensor. They can be separated using the FT shown in Fig. 5b by assuming that the components at the harmonic frequencies of $f = 2nk/\lambda_{Laser}$ (where $k = 1, 2, 3, 4, …$) are from the nonlinearity of the $z$-interferometer, whereas the remaining components are from the nonlinearity of the capacitive sensor. The characterized spectrum of the nonlinearity of the $z$-interferometer in Fig. 5b is very similar to that of Fig. 3d, with the 4th-order nonlinearity component being the most dominant one.

With the inverse FT of the characterized components at the harmonic frequencies, we can easily obtain the nonlinearity error of the $z$-interferometers shown as the red curve in Fig. 5a. Similarly, with the inverse FT of the remaining components, we can get a curve, as shown in Fig. 5c, which represents the nonlinearity of the capacitive sensor and the tracking error of the measurement.

The characterization measurements mentioned above were repeated six times. The characterized nonlinearity curves of the $z$-interferometers are plotted in Fig. 6a. Their averaged curve is plotted in Fig. 6b in black (left $y$-axis), and their standard deviation curve is plotted in purple (right $y$-axis). The standard deviation is approximately 0.15 nm, slightly worse than the calibration results using a flat surface, as shown in Fig. 4a. The main reason is due to the influence of the nonlinearity of the capacitive sensor and the tracking error of the AFM controller.

An advantage of applying this method in our Met. LR-AFM is that it can be carried out in situ. With a software
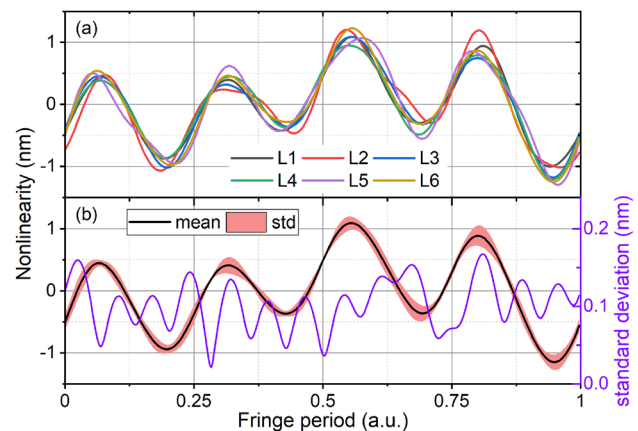


**Fig. 6** Experimental result of the high-order nonlinearity correction using the embedded capacitive sensor: **a** nonlinearity curves characterized by six independent measurement runs; **b** averaged nonlinearity curve of the curves shown in **a** and their standard deviation curve

Fig. 1, the sum of the values of the $z$-axis interferometer and the values of the capacitive sensor should be constant. By simultaneously recording the values of the two sensors in

function developed in our measurement software, such a characterization process can be completed in a few seconds. In addition, the quality of the sample applied in the characterization process has almost no influence on the characterization performance, as a fixed position of the sample is detected in the measurement process. Consequently, the characterization can be conveniently performed on any samples under calibration.

### 3.3 Correction of the High-Order Nonlinearity Error

After the nonlinearity error is characterized, it can be applied as a look-up table for correction. We developed two software modules integrated into the measurement software of Met. LR-AFM. One module is for characterizing the nonlinearity error using one of the two methods introduced above, which can be configured in the software. Nonlinearity errors up to the 16th order can be characterized using the software module, which is far more than needed. The module outputs the characterized nonlinearity error parameters, i.e., the amplitude and phase of 16 orders of nonlinearity errors, which can be either saved or directly applied for error correction. The other module is for correcting the nonlinearity error. Nonlinearity error parameters from either fresh measurements or previous characterizations can be loaded in the module. Fresh measurements here mean that the characterization of the nonlinearity error is performed just before the correction function is activated. After loading the nonlinearity error parameters, a look-up table of the nonlinearity error curve will be calculated and applied to the measurements in situ. The whole procedure is automatic, so the characterization and correction method proposed in this paper can be applied very conveniently by a normal staff.

To demonstrate the performance of the nonlinearity error correction, the flat surface shown in Fig. 3 was measured

again with the activated nonlinearity error correction function. The measured topography after the plane correction is shown in Fig. 7a, with a cross-sectional profile shown in Fig. 7b. Clearly, the cyclic artifact shown in Fig. 3 has been fully removed, indicating the effectiveness of the developed method. Moreover, two large peaks in the image are due to contaminations on the surface.

## 4 Propagation of the (Residual) Nonlinearity Error in the Step Height and Etching Depth Calibrations

This section aims to study how the (residual) nonlinearity error influences the step height and etching depth calibrations. As the nonlinearity error is in a nonlinear function of the coordinates of the measured pixels, such an analysis is not straightforward. We performed a specially designed measurement experiment to present an intuitive illustration of its error propagation, as shown in Fig. 8a. In the experiment, the sample was well aligned along the $x$-axis (fast scan axis) without a tilting angle, and it was slightly inclined with an angle (0.44°) along the $y$-axis (slow scan axis). Figure 8a shows the measured AFM image as the raw data. According to ISO5436, the data evaluation was performed line by line, as shown in Fig. 8b, where the height offsets between the middle segment ($C$) at the top and two segments ($A$ and $B$) at the bottom are calculated as the feature height $h$. The segments $A$, $B$, and $C$ typically have a length of $w/3$ and a distance to the edge of the structure of $w/3$, where $w$ is the width of the structure. $h$ can be denoted as

$$h = \overline{z_C(x, y)} - \frac{\overline{z_A(x, y)} + \overline{z_B(x, y)}}{2}, \tag{3}$$

**Fig. 7** Measurement results of a flat surface after the correction of the high-order nonlinearity errors
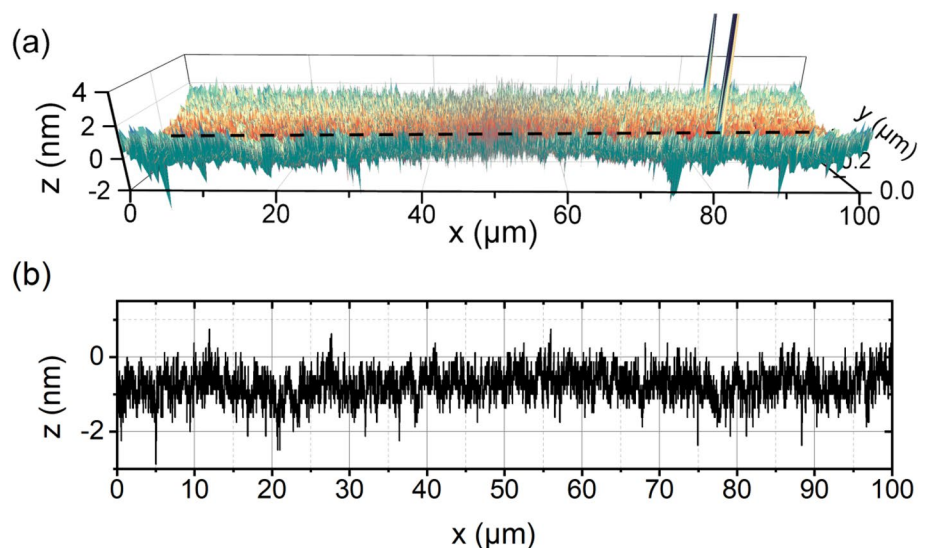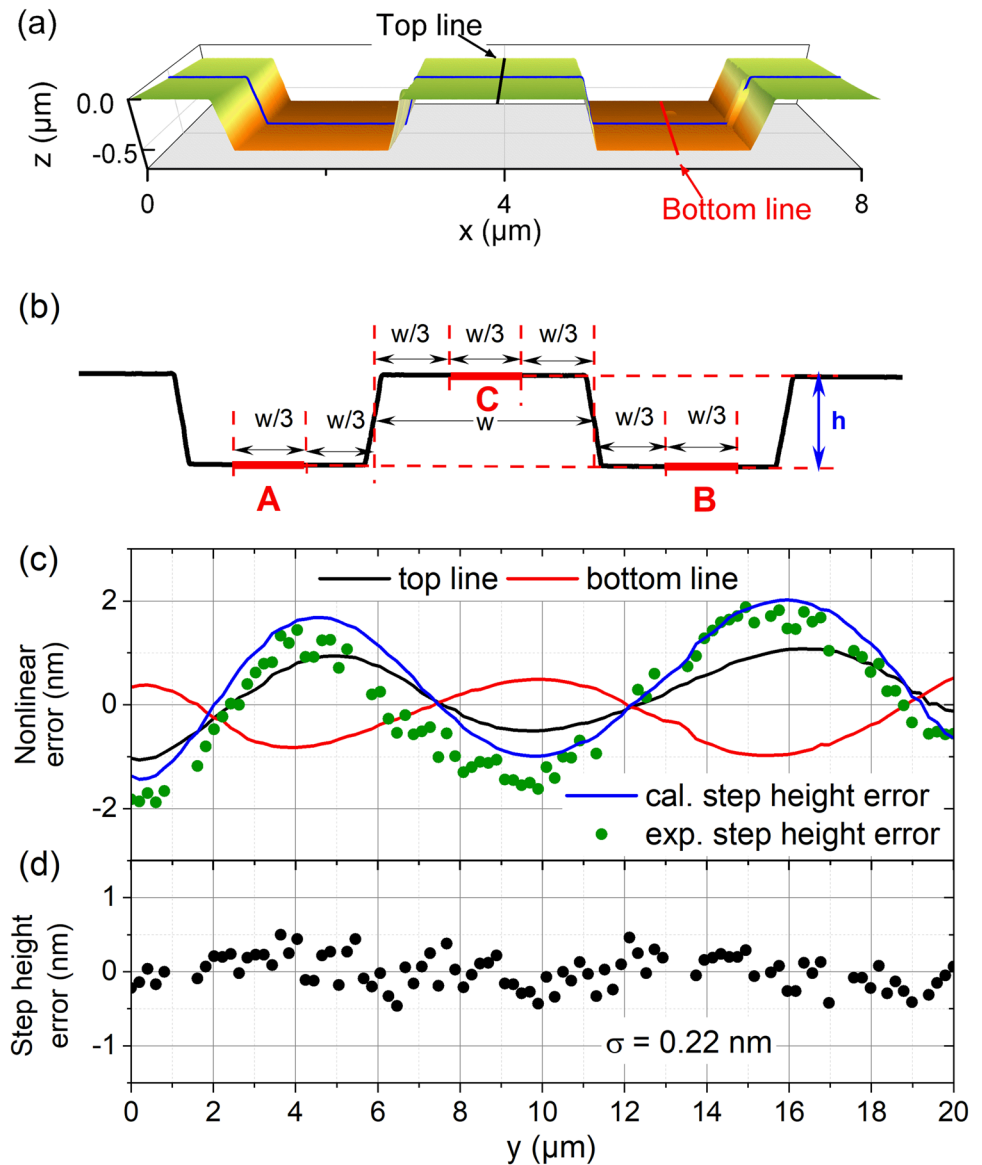
**Fig. 8** Measurement results of the propagation of the nonlinearity error in the step height calibration. See text for details



where $\overline{z_A(x,y)}$, $\overline{z_B(x,y)}$, and $\overline{z_C(x,y)}$ indicate the averaged $z$ coordinates of segments $A$, $B$, and $C$, respectively.

The propagated error contribution of the interferometric nonlinearity error on $h$ can be written as

$$u = \overline{N_z[z_C(x,y)]} - \frac{\overline{N_z[z_A(x,y)]} + \overline{N_z[z_B(x,y)]}}{2}, \qquad (4)$$

where $N_z(z)$ indicates the nonlinearity error of the $z$-interferometer at the height of $z$ and $\overline{N_z[z_I(x,y)]}$ indicates the averaged nonlinearity errors of all pixels at segment $I$, where $I = A$, $B$, or $C$.

As the sample was perfectly aligned along the $x$-axis in the experiment, the propagated error $u$ at each line can be simplified as the difference between the nonlinearity errors at the center points of segments $C$ and $B$. Thus, the overall

propagated error on all scan lines can be evaluated as the difference of nonlinearity errors at the top line (black) and bottom line (red) in Fig. 8a. As the sample was (slightly) titled along the $y$-axis, its $z$ coordinates $z_t(x_t, y)$ and $z_b(x_b, y)$ changed with respect to the $y$-coordinate along two lines. Consequently, $y$-dependent nonlinearity errors will be introduced, as plotted in Fig. 8c as black and red lines. Such nonlinearity errors lead to the height measurement error, plotted as the blue solid curve in Fig. 8c. For comparison, the experimentally measured feature height variation is shown as green dots. The simulated and experimental results agree very well. The error contribution has an amplitude of over 3 nm, showing a significant influence on the step height calibration due to the interferometric nonlinearity error.

To indicate the effectiveness of the developed method, the measured feature height after applying the nonlinearity

**Fig. 9** Calibrated results of a highly demanding industrial sample as an example. The results slightly vary at different measurement positions owing to the sample inhomogeneity
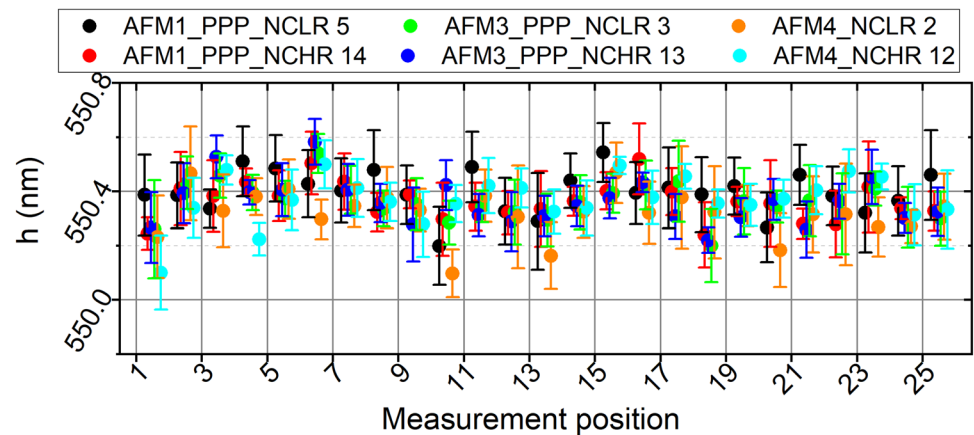


error correction method is plotted in Fig. 8d. The measurement results become much more stable due to the reduced nonlinearity error.

## 5 Performance of the Step Height and Etching Depth Calibration after the Improvement

The performance of the state-of-the-art Met. LR-AFM after applying the developed method was carefully verified in the calibration service of several highly demanding industrial samples. One set of results was introduced already in [12], and another set of results is depicted in Fig. 9. The sample was measured at 25 different positions in the calibration. Six groups of measurements were performed with three different AFM heads (AFM1, AFM3, and AFM4) and six different AFM probes (three with the type PPP_NCLR and three with the type PPP-NCHR, all from Nanosensors™). The results of each measurement position are highly repeatable, but they slightly differ between different measurement positions owing to the sample inhomogeneity. We evaluated six mean height values from six groups of measurements. Their standard deviation reached 0.03 nm. The standard deviation of all 150 results, i.e., 6 groups × 25 results per group, was 0.08 nm, which includes the contributions from the reproducibility of the metrology tool and the sample inhomogeneity.

With the research achievements, we can now perform step height and etching depth calibration with an expanded measurement uncertainty ($k=2$) down to $U=0.3$ nm. This result is a significant improvement compared to our previous calibration uncertainty $U$ of approximately 1.0–2.0 nm.

## 6 Conclusions

In summary, this paper introduces a challenging problem concerning the high-order nonlinearity errors of interferometers in the Met. LR-AFM of the PTB, which were not properly corrected by the well-known Heydemann correction method. To solve this problem, two new correction methods are proposed, one using a physical artifact with a flat surface and another using a capacitive sensor embedded in the Met. LR-AFM. The experimental results show that the methods can effectively reduce the nonlinearity error, for instance, down to 0.03 nm, when a high-quality crystal silicon surface is applied. Furthermore, the propagation of the (residual) nonlinearity error in the step height calibration was examined. Finally, the metrology performance of the Met. LR-AFM in the calibration of a highly demanding industrial sample was verified: the standard deviation of six groups of reproducible measurements reached 0.03 nm. The developed method can be applied conveniently in the measurement process.

Nonetheless, only the nonlinearity error of the *z*-interferometer has been focused on in this paper as the performance of the *z*-interferometer is much more critical than the *x*- and *y*-interferometers in the step height and etching depth calibrations. The proposed method can be expanded for the interferometers of the other axes, but it needs an AFM probe that can probe along the *x*- or *y*-axis. Such a probe can be an assembled cantilever probe [19], a flared CD-AFM probe [20], or a 3D nanoprobe [21].

Using the proposed method in this publication, the nonlinearity error curve needs to be characterized before being applied as a look-up table for correction. This fact implies a precondition to apply the method: the nonlinearity status of the interferometer should be stable over its measurement range and measurement time. This precondition can be well satisfied in optical interferometers embedded in metrological AFMs due to their stable mechanical and optical constructions, among others. The stability of the

nonlinearity error curves characterized at different time over a few weeks, shown in Figs. 4 and 6, proved this issue.

## Declarations

**Conflict of interest** The paper has no conflict of interest.

## References

1. Dai G, Park D, Orji NG (2022) Foreword to the special issue on atomic and close-to-atomic scale metrology. Nanomanuf Metrol 5:81–82
2. Dai G, Koenders L, Flügge J, Bosse H (2016) Two approaches for realizing traceability in nanoscale dimensional metrology. Opt Eng 55:091407
3. Wilkening G, Koenders L (2005) Nanoscale calibration standards and methods: dimensional and related measurements in the micro and nanometer range. Wiley-VCH, Weinheim
4. Buhr E, Michaelis W, Diener A, Mirande W (2007) Multi-wavelength VIS/UV optical diffractometer for high-accuracy calibration of nano-scale pitch standards. Meas Sci Technol 18:667–674
5. Haitjema H (1997) International comparison of depth-setting standards. Metrologia 34:161
6. Dai G, Wolff H, Pohlenz F, Danzebrink HU (2009) A metrological large range atomic force microscope with improved performance. Rev Sci Instrum 80:043702
7. Gonda S, Doi T, Kurosawa T, Tanimura Y, Hisata N, Yamagishi T, Fujimoto H, Yukawa H (1999) Real-time, interferometrically measuring atomic force microscope for direct calibration of standards. Rev Sci Instrum 70:3362
8. Picotto GB, Pisani M (2001) A sample scanning system with nanometric accuracy for quantitative SPM measurements. Ultramicroscopy 86:247
9. Meli F, Thalmann R (1998) Long-range AFM profiler used for accurate pitch measurements. Meas Sci Technol 9:1087
10. Benkler E, Rohde F, Telle HR (2013) Robust interferometric frequency lock between CW lasers and optical frequency combs. Opt Lett 38:555–557
11. Koenders L, Klapetek P, Meli F, Picotto GB (2006) Comparison on step height measurements in the nano and micrometre range by scanning force microscopes. Metrologia 43:04001
12. Dai G, Hu XK (2022) Progress in nanometrology: reduction of measurement uncertainty of step height and etching depth calibration down to 0.3 nm. In: Proceeding of Euspen's 22nd international conference and exhibition, Geneva, CH
13. Dai G, Pohlenz F, Danzebrink UU, Xu M, Hasche K, Wilkening G (2004) Metrological large range scanning probe microscope. Rev Sci Instrum 75:962
14. Manske E, Hausotte T, Jäger G (2007) New applications of the nanopositioning and nanomeasuring machine by using advanced tactile and non-tactile probes. Meas Sci Technol 18:520
15. Dai G, Zhu F, Fluegge J (2015) High-speed metrological large range AFM. Meas Sci Technol 26:095402
16. Dai G, Pohlenz F, Wilkening G (2004) Improving the performance of interferometers in metrological scanning probe microscopes. Meas Sci Technol 15:444–450
17. Heydemann P (1981) Determination and correction of quadrature fringe measurement errors in interferometers. Appl Opt 20:3382
18. Bridges A, Yacoot A, Kissinger T, Humphreys DA, Tatam RP (2021) Correction of periodic displacement non-linearities by two-wavelength interferometry. Meas Sci Technol 32:125202
19. Dai G, Wolff H, Weimann T, Xu M, Pohlenz F, Danzebrink H-U (2007) Nanoscale surface measurements at sidewalls of nano- and micro-structures. Meas Sci Technol 18:334–341
20. Dai G, Häßler-Grohne W, Hüser D et al (2012) New developments at Physikalisch Technische Bundesanstalt in three-dimensional atomic force microscopy with tapping and torsion atomic force microscopy mode and vector approach probing strategy. J Micro/Nanolithogr MEMS MOEMS 11:011004
21. Thiesler J, Ahbe T, Tutsch R, Dai G (2022) True 3D nanometrology: 3D-probing with a cantilever-based sensor. Sensors 22:314